

REPORT DOCUMENTATION PAGE			Form Approved OMB NO. 0704-0188		
<p>The public reporting burden for this collection of information is estimated to average 1 hour per response, including the time for reviewing instructions, searching existing data sources, gathering and maintaining the data needed, and completing and reviewing the collection of information. Send comments regarding this burden estimate or any other aspect of this collection of information, including suggestions for reducing this burden, to Washington Headquarters Services, Directorate for Information Operations and Reports, 1215 Jefferson Davis Highway, Suite 1204, Arlington VA, 22202-4302. Respondents should be aware that notwithstanding any other provision of law, no person shall be subject to any penalty for failing to comply with a collection of information if it does not display a currently valid OMB control number. PLEASE DO NOT RETURN YOUR FORM TO THE ABOVE ADDRESS.</p>					
1. REPORT DATE (DD-MM-YYYY)		2. REPORT TYPE		3. DATES COVERED (From - To)	
		New Reprint		-	
4. TITLE AND SUBTITLE			5a. CONTRACT NUMBER		
Numerical simulation of flow overurban-like topographies and evaluationof turbulence temporal attributes			W911NF-13-1-0474		
			5b. GRANT NUMBER		
			5c. PROGRAM ELEMENT NUMBER		
			611102		
6. AUTHORS			5d. PROJECT NUMBER		
William Anderson, Qi Li, Elie Bou-Zeid					
			5e. TASK NUMBER		
			5f. WORK UNIT NUMBER		
7. PERFORMING ORGANIZATION NAMES AND ADDRESSES			8. PERFORMING ORGANIZATION REPORT NUMBER		
Baylor University					
One Bear Place 97360					
Waco, TX			76798 -7360		
9. SPONSORING/MONITORING AGENCY NAME(S) AND ADDRESS (ES)			10. SPONSOR/MONITOR'S ACRONYM(S)		
U.S. Army Research Office			ARO		
P.O. Box 12211			11. SPONSOR/MONITOR'S REPORT NUMBER(S)		
Research Triangle Park, NC 27709-2211			63209-EV.3		
12. DISTRIBUTION AVAILABILITY STATEMENT					
Approved for public release; distribution is unlimited.					
13. SUPPLEMENTARY NOTES					
The views, opinions and/or findings contained in this report are those of the author(s) and should not contrued as an official Department of the Army position, policy or decision, unless so designated by other documentation.					
14. ABSTRACT					
We have used large-eddy simulation with an immersed boundary method to study turbulent flows over distributions of uniform height, staggered cubes. The computational domains were designed such that both the roughness sublayer and a region of the inertial layer are resolved. With this, we record vertical profiles of time series of fluctuating streamwise and vertical velocity at different locations throughout the domain. Contour images of these fluctuating quantities shown relative to elevation and time are studied; contour images of Reynolds shear stresses owing to 'swings' and 'suctions' are also studied. These images show that periods of momentum excess (deficit)					
15. SUBJECT TERMS					
large-eddy simulation; roughness sublayer; atmospheric surface layer; coherent motions; hairpin packets; advective lag					
16. SECURITY CLASSIFICATION OF:			17. LIMITATION OF	15. NUMBER	19a. NAME OF RESPONSIBLE PERSON
a. REPORT	b. ABSTRACT	c. THIS PAGE	ABSTRACT	OF PAGES	William Anderson
UU	UU	UU	UU		19b. TELEPHONE NUMBER
					972-883-4660

## Report Title

Numerical simulation of flow over urban-like topographies and evaluation of turbulence temporal attributes

### ABSTRACT

We have used large-eddy simulation with an immersed boundary method to study turbulent flows over distributions of uniform height, staggered cubes. The computational domains were designed such that both the roughness sublayer and a region of the inertial layer are resolved. With this, we record vertical profiles of time series of fluctuating streamwise and vertical velocity at different locations throughout the domain. Contour images of these fluctuating quantities shown relative to elevation and time are studied; contour images of Reynolds shear stresses owing to 'sweeps' and 'ejections' are also studied. These images show that periods of momentum excess (deficit) in the inertial-layer precede excitation (subdual) of cube-scale coherent vortices in the roughness sublayer. We compute this time lag (termed advective lag) and demonstrate that it scales linearly with wall-normal elevation. The advective lag is attributed to coherent, low- and high-momentum regions in the aloft inertial layer. Vortex identification is used to illustrate the presence of hairpin packets encapsulating low-momentum regions. Based on this, the reported inclination angle associated with hairpin packets is used to guide the development of a model for prediction of advective lag with height. The model captures the advective lag profiles reasonably well. In the interest of generality, additional cases of flow over homogeneous roughness (aerodynamic drag imposed with the equilibrium logarithmic law) are considered. We again observe that advective lag scales linearly with wall-normal elevation. Advective lag predictions from the aforementioned model agree well with results for these cases.

---

**REPORT DOCUMENTATION PAGE (SF298)**  
**(Continuation Sheet)**

---

Continuation for Block 13

ARO Report Number 63209.3-EV  
Numerical simulation of flow overurban-like topc..

Block 13: Supplementary Note

© 2015 . Published in Journal of Turbulence, Vol. Ed. 0 16, (9) (2015), (, (9). DoD Components reserve a royalty-free, nonexclusive and irrevocable right to reproduce, publish, or otherwise use the work for Federal purposes, and to authorize others to do so (DODGARS §32.36). The views, opinions and/or findings contained in this report are those of the author(s) and should not be construed as an official Department of the Army position, policy or decision, unless so designated by other documentation.

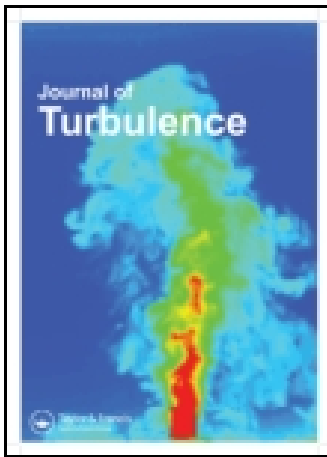
Approved for public release; distribution is unlimited.

This article was downloaded by: [Princeton University]

On: 15 May 2015, At: 09:53

Publisher: Taylor & Francis

Informa Ltd Registered in England and Wales Registered Number: 1072954 Registered office: Mortimer House, 37-41 Mortimer Street, London W1T 3JH, UK



## Journal of Turbulence

Publication details, including instructions for authors and subscription information:

<http://www.tandfonline.com/loi/tjot20>

### Numerical simulation of flow over urban-like topographies and evaluation of turbulence temporal attributes

William Anderson<sup>a</sup>, Qi Li<sup>b</sup> & Elie Bou-Zeid<sup>b</sup>

<sup>a</sup> Mechanical Engineering Department, The University of Texas at Dallas, Richardson, TX, USA

<sup>b</sup> Department of Civil and Environmental Engineering, Princeton University, Princeton, NJ, USA

Published online: 13 May 2015.



CrossMark

[Click for updates](#)

**To cite this article:** William Anderson, Qi Li & Elie Bou-Zeid (2015) Numerical simulation of flow over urban-like topographies and evaluation of turbulence temporal attributes, Journal of Turbulence, 16:9, 809-831, DOI: [10.1080/14685248.2015.1031241](https://doi.org/10.1080/14685248.2015.1031241)

**To link to this article:** <http://dx.doi.org/10.1080/14685248.2015.1031241>

PLEASE SCROLL DOWN FOR ARTICLE

Taylor & Francis makes every effort to ensure the accuracy of all the information (the "Content") contained in the publications on our platform. However, Taylor & Francis, our agents, and our licensors make no representations or warranties whatsoever as to the accuracy, completeness, or suitability for any purpose of the Content. Any opinions and views expressed in this publication are the opinions and views of the authors, and are not the views of or endorsed by Taylor & Francis. The accuracy of the Content should not be relied upon and should be independently verified with primary sources of information. Taylor and Francis shall not be liable for any losses, actions, claims, proceedings, demands, costs, expenses, damages, and other liabilities whatsoever or howsoever caused arising directly or indirectly in connection with, in relation to or arising out of the use of the Content.

This article may be used for research, teaching, and private study purposes. Any substantial or systematic reproduction, redistribution, reselling, loan, sub-licensing, systematic supply, or distribution in any form to anyone is expressly forbidden. Terms &

Conditions of access and use can be found at <http://www.tandfonline.com/page/terms-and-conditions>

## Numerical simulation of flow over urban-like topographies and evaluation of turbulence temporal attributes

William Anderson<sup>a\*</sup>, Qi Li<sup>b</sup> and Elie Bou-Zeid<sup>b</sup>

<sup>a</sup>Mechanical Engineering Department, The University of Texas at Dallas, Richardson, TX, USA;

<sup>b</sup>Department of Civil and Environmental Engineering, Princeton University, Princeton, NJ, USA

(Received 24 October 2014; accepted 15 March 2015)

We have used large-eddy simulation with an immersed boundary method to study turbulent flows over distributions of uniform height, staggered cubes. The computational domains were designed such that both the roughness sublayer and a region of the inertial layer are resolved. With this, we record vertical profiles of time series of fluctuating streamwise and vertical velocity at different locations throughout the domain. Contour images of these fluctuating quantities shown relative to elevation and time are studied; contour images of Reynolds shear stresses owing to ‘sweeps’ and ‘ejections’ are also studied. These images show that periods of momentum excess (deficit) in the inertial-layer precede excitation (subdual) of cube-scale coherent vortices in the roughness sublayer. We compute this time lag (termed advective lag) and demonstrate that it scales linearly with wall-normal elevation. The advective lag is attributed to coherent, low- and high-momentum regions in the aloft inertial layer. Vortex identification is used to illustrate the presence of hairpin packets encapsulating low-momentum regions. Based on this, the reported inclination angle associated with hairpin packets is used to guide the development of a model for prediction of advective lag with height. The model captures the advective lag profiles reasonably well. In the interest of generality, additional cases of flow over homogeneous roughness (aerodynamic drag imposed with the equilibrium logarithmic law) are considered. We again observe that advective lag scales linearly with wall-normal elevation. Advective lag predictions from the aforementioned model agree well with results for these cases.

**Keywords:** large-eddy simulation; roughness sublayer; atmospheric surface layer; coherent motions; hairpin packets; advective lag

### 1. Introduction and motivation

The dynamics of turbulent flows over rough walls are important in numerous settings. The performance of vapour power systems,[1] the efficiency of naval vessels,[2] and the economics of pipeline transport are the examples of contemporary applications greatly influenced by turbulent momentum exchanges in close proximity to the wall. Meanwhile, turbulent momentum transport in atmospheric boundary layer flows is of critical importance to the performance of modern wind farms,[3] aerodynamics of vegetative canopies [4,5] and urban environments,[6–9] and geomorphological processes associated with the evolution of aeolian desert landscapes.[10] The aforementioned engineering and geophysical examples are distinctly different to smooth wall turbulence, owing to the presence of a distribution of obstacles of height,  $h$ , that protrude into the inertial layer of the flow. These obstacles

---

\*Corresponding author. Email: [wca140030@utdallas.edu](mailto:wca140030@utdallas.edu)

absorb momentum through pressure drag, induce flow separation, and serve to produce obstacle-scale coherent motions that occupy the region between the wall and approximately three obstacle heights above the roughness sublayer.[11,12] In the roughness sublayer, the aerodynamic drag distribution due to the presence of obstacles results in an inflected mean streamwise velocity profile at the approximate average obstacle height.[13,14] As a result, the mean flow gradient exhibits its maxima at the inflection [10] (not the wall), and the turbulence kinematics are fundamentally different. For flow over vegetative canopies, Raupach et al. [15] demonstrated that flow in the roughness sublayer resembled a turbulent mixing layer with positively and negatively skewed streamwise and vertical velocity fluctuations, respectively, and Reynolds stresses composed predominately of ‘sweeps’. With this, the turbulence structure is characterised by Kelvin–Helmholtz spanwise ‘rollers’, which originate at the velocity profile inflection and undergo a downstream transformation leading to hairpin packets [4] (while remaining contained within the roughness sublayer). Recently, Ghisalberti [16] demonstrated the existence of an universality in roughness sublayer statistics for flows over diverse canopies, and introduced the term ‘*obstructed shear flow*’ to categorise such flows. Within the sublayer, the turbulence geometric macroscale is set by the vorticity thickness,[15,17]  $\delta_w = U(h)/(dU(z)/dz)|_h$ , and streamwise spacing of vortex cores,  $\Lambda_x = 2\pi L_{\dot{w}}$ , where  $U(z)$  and  $L_{\dot{w}}$  is the mean streamwise velocity and the integral length scale, respectively.<sup>1</sup> The mixing efficiency associated with these Kelvin–Helmholtz roughness sublayer motions – which is commonly quantified via the correlation coefficient,  $r_{uw} = u_\tau^2/u_{\text{rms}}w_{\text{rms}}$ , where  $u_\tau$  is friction velocity and rms denotes root mean square – exceeds the value exhibited by a logarithmic boundary layer by approximately 50%.[16,18] Thus, turbulence in the roughness sublayer is characterised by vigorous mixing and complex structural attributes.

Above the roughness sublayer – in the inertial layer – the mean flow profile exhibits logarithmic scaling and the turbulence structure resembles smooth wall flow.[8,13,14] That is, the domain is occupied by persistent streamwise-elongated coherent parcels of relatively low and high momentum. For smooth walls, such low-momentum regions (LMRs) meander,[19] and are encapsulated by hairpin packets [20–27] at the interface between zones of quasi-uniform momentum.[28] For rough walls, the presence of persistent structures is also reported,[8,25] however, experiments have indicated that  $h$ -scale coherent motions associated with the roughness sublayer seemingly reduce the lengths of logarithmic-layer coherent motions.[25,29] Recently, Coceal et al. [8] used direct numerical simulation (DNS) to study flow over a staggered array of uniform height cubes [6] with characteristic scale,  $h/H = \frac{1}{4}$ , where  $H$  is the boundary layer depth. They illustrated the existence of hairpin packets (and ‘cane’ structures, which are inclined coherent parcels with only one leg of the hairpin [24] around the LMR). Moreover, they used approximated conditional averages [20,30] to illustrate the significant reductions in streamwise coherence of their rough wall turbulence relative to a smooth wall. These efforts to characterise the structural attributes of smooth and rough wall turbulence have typically focused on spatial characteristics. Furthermore, most previous studies address either instantaneous, ensemble-averaged or time-averaged statistically stationary turbulence statistics. Here, we have used large-eddy simulation (LES) to study the temporal dynamics of turbulent flows over such roughness. This is accomplished by recording time-series flow statistics across the depth of the boundary layer at a variety of horizontal positions (thus, we use LES to generate data-sets that would more typically be associated with field campaign data from a tower equipped with sonic anemometers).[31] An advantage of our approach is that it would provide insight into the interpretation of laboratory or field experimental results, which are often collected as

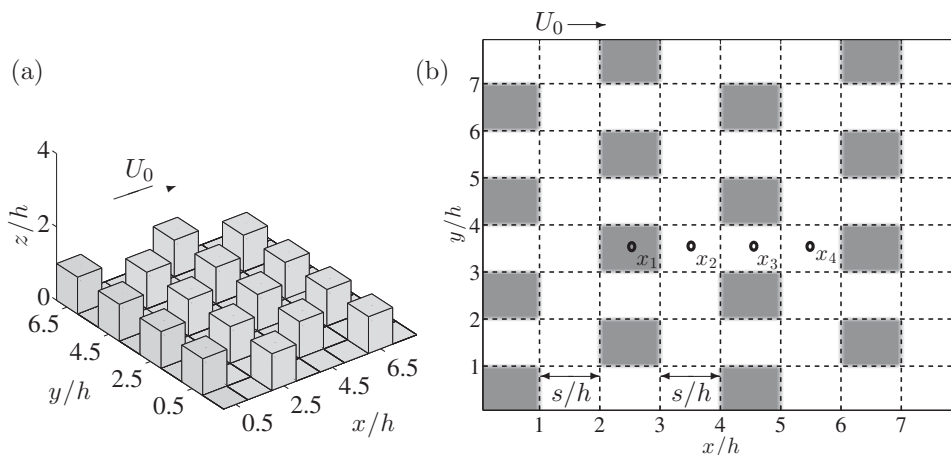


Figure 1. Illustration of [6] block case ('C20S') considered as lower topography in this study: (a) perspective image showing freestream flow direction,  $U_0$  and (b) planform image with indication of positions at which time–height velocity data are recorded. Owing to the topography attributes, the four points effectively capture temporal dynamics at all points in the domain. The above topography is labelled here Case SC2.

time series. Moreover, illustrations of ‘time–height’ colour floods of fluctuating streamwise velocity offer a novel perspective on the presence of the aforementioned coherent flow structures and clearly show the extent to which activity in the roughness sublayer is influenced by inertial-layer dynamics. Moreover, by incorporating these results with arguments relating to structural attributes of coherent flow structures in wall-bounded flows, we have been able to develop a predictive model for the reported advective lag. We stress that the results presented here (and related predictive capability) are not expected to apply only to flow over urban-like complex topographies. Thus, the predictive capability could be used, for example, in conjunction with an atmospheric LiDAR system for control of wind farms.

### 1.1. Present study

We use LES to model flow over topographies composed of a staggered distribution of wall-mounted cubes (one of the cases considered is ‘C20S’ from the wind tunnel study by Cheng and Castro [6], and considered in the more recent DNS study by Coceal et al. [8]). Figure 1(a) shows a perspective view of the array of cubes with edge length,  $h$ . Figure 1(b) shows the arrangement in planform, with indication of the streamwise spacing,  $s/h$ , between rows of cubes ( $s/h = 1$  for all cases in this study). Figure 1(b) includes points  $x_1$ ,  $x_2$ ,  $x_3$ , and  $x_4$ ; during LES, time series of streamwise and vertical velocity have been recorded across the depth of the boundary layer at these points. This is better illustrated in Figure 2(a), which shows the cubes and streamwise spacing (for the cube cases, the  $y$  coordinates of positions  $x_1$ – $x_4$  are equal and set to intersect the centre of cubes; the  $x$  coordinates are varied such that  $x_1$  is precisely at the centre of a cube,  $x_2$  is centred between the upwind and downwind row of cubes,  $x_3$  is precisely at the centre of adjacent cubes, and  $x_4$  is centred between the upwind and downwind row of cubes). For generality, we also model flow over homogeneous roughness lengths, shown in Figure 2(b). The novelty of this work resides in the insights gained from considering time–height contours of fluctuating velocity components in the context of the aforementioned (and comprehensively studied) structural

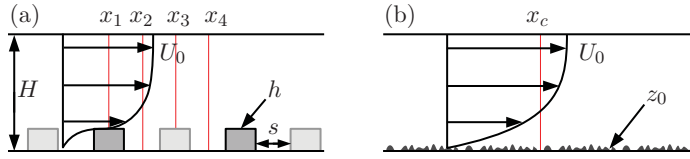


Figure 2. Illustration of computational domains considered in this study: (a) uniform height, staggered array of blocks [6] with  $h$  varying,  $s/h = 1$  and (b) homogeneous roughness,  $z_0$ . For panel (a), see also Figure 1. For all cases,  $H = 1000$  m and other simulation parameters are summarised in Table 1. Illustrative locations of positions at which time series of streamwise and vertical velocity are recorded are shown for discussion (vertical red lines). In both, an illustrative time-averaged streamwise velocity profile is shown, where  $U_0$  is the ‘outer’ freestream velocity.

attributes [8,20–22] of turbulence in the roughness sublayer [8,25] and inertial layer. The results (Sections 3.1–3.3) and scaling arguments (Section 3.4) demonstrate the influence of inertial-layer structures on dynamics of the roughness sublayer. Section 2 contains a description of the LES code and validation against an available wind tunnel data-set [6]; a description of the cases considered for this study is also provided in Sections 2. Section 3 shows a series of results that lead to a semi-empirical model for reported temporal dynamics of the urban sublayer. The influence of resolution (spatial and temporal) is tested in Section 3.5; we report that advective lag does not exhibit dependence on resolution. Concluding remarks are provided in Section 4.

## 2. Method and cases

We consider flow over Figure 2(a) and 2(b) topographies with attributes summarised in Table 1. During LES, the spatially filtered three-dimensional incompressible momentum transport equations are solved at high-Reynolds number [32–35] for a neutrally stratified (i.e. no buoyancy forces) turbulent boundary layer without Coriolis accelerations:

$$\frac{\partial \tilde{\mathbf{u}}}{\partial t} + \frac{1}{2} \nabla (\tilde{\mathbf{u}} \cdot \tilde{\mathbf{u}}) - \tilde{\mathbf{u}} \times \tilde{\boldsymbol{\omega}} = -\frac{1}{\rho} \nabla \tilde{p} - \nabla \cdot \boldsymbol{\tau} + \Pi + \frac{1}{\rho} \mathbf{f}, \quad (1)$$

where  $\tilde{p}$  is the modified pressure,  $\boldsymbol{\tau}$  is the subgrid-scale (SGS) stress tensor, and  $\Pi = \{u_\tau^2/H, 0, 0\}$  is the mean pressure gradient in the streamwise direction, where  $u_\tau$  is the shear velocity ( $u_\tau = 0.45$  m/s) and  $H$  is the boundary layer depth ( $H = 1000$  m). A solenoidal

Table 1. Summary of simulation parameters and domain attributes. For all cases,  $H = 1000$  m.

Description	Name	$L/H$	$h/H$	$z_0/H$	$N_x \times N_y \times N_z$
Staggered cubes	SC1	4	1/8	$2 \times 10^{-5}$	$128 \times 128 \times 128$
Staggered cubes	SC2	2	1/4	$2 \times 10^{-5}$	$128 \times 128 \times 128$
Uniform roughness	U1	4	–	$1 \times 10^{-3}$	$128 \times 128 \times 128$
Uniform roughness	U2	4	–	$1 \times 10^{-2}$	$64 \times 64 \times 64$
Uniform roughness	U3	4	–	$1 \times 10^{-3}$	$64 \times 64 \times 64$
Uniform roughness	U4	4	–	$1 \times 10^{-4}$	$64 \times 64 \times 64$
Uniform roughness	U5	4	–	$1 \times 10^{-5}$	$64 \times 64 \times 64$
Uniform roughness	U6	4	–	$1 \times 10^{-6}$	$64 \times 64 \times 64$

velocity field is maintained by computing the divergence of Equation (1), applying the incompressibility condition,  $\nabla \cdot \tilde{\mathbf{u}} = 0$ , and solving the resulting pressure Poisson equation for a pressure correction. Note also that the viscous stresses,  $\nu \nabla^2 \tilde{\mathbf{u}}$ , are omitted from Equation (1), owing to the high-Reynolds number typical of atmospheric surface layer flows (the ‘macroscale’ Reynolds number is  $\text{Re}_\tau = U_0 H / \nu \sim \mathcal{O}(10^9)$ ). The deviatoric component of  $\tau_{ij}$  is evaluated using the eddy viscosity modelling approach,

$$\boldsymbol{\tau} - \frac{1}{3} \delta \text{Tr}(\boldsymbol{\tau}) = -2\nu_t \tilde{\mathbf{S}}, \quad (2)$$

where  $\nu_t = (C_s \Delta)^2 |\tilde{\mathbf{S}}|$  is the turbulent viscosity,  $C_s$  is the Smagorinsky coefficient, [36]  $\Delta$  is the filter size,  $\tilde{\mathbf{S}} = \frac{1}{2}(\nabla \tilde{\mathbf{u}} + \nabla \tilde{\mathbf{u}}^{\text{Tr}})$  is the resolved strain-rate tensor, and  $|\tilde{\mathbf{S}}| = (2\tilde{\mathbf{S}}:\tilde{\mathbf{S}})^{1/2}$  is magnitude of the resolved strain-rate tensor. For this work,  $C_s$  is evaluated dynamically during LES with the Lagrangian scale-dependent dynamic SGS model of Bou-Zeid et al. [34]. Pseudospectral discretisation is used in the horizontal directions, while vertical gradients are evaluated with centred second-order finite differencing. Periodic boundary conditions are imposed on the vertical planes of the domain, owing to spectral discretisation in the horizontal directions. At the domain top, the zero-stress Neumann boundary condition is imposed on streamwise and spanwise velocity,  $\partial \tilde{u} / \partial z|_{z/H=0} = \partial \tilde{v} / \partial z|_{z/H=0} = 0$ . The zero vertical velocity condition is imposed at the domain top and bottom,  $\tilde{w}(x, y, z/H = 0) = \tilde{w}(x, y, z/H = 1) = 0$ . Zero-stress Neumann boundary conditions are imposed on the pressure Poisson equation solution at the domain top and bottom,  $\partial \tilde{p} / \partial z|_{z/H=0} = \partial \tilde{p} / \partial z|_{z/H=1} = 0$ . The Adams–Bashforth time-advancement scheme is used for temporal integration of Equation (1). The nonlinear advection term is de-aliased in Fourier space with the 3/2 rule [37]; this is necessary since aliasing errors may contaminate the smallest resolved scales of the flow, compromising predictions of the SGS models. The computational domain discretisation is  $\Delta_x = \Delta_y = L_x / N_x$ , and  $\Delta_z = H / N_z$ , where  $L$  is indicated in Table 1 and  $N_x = N_y = N_z$ . The computational domain is staggered in the vertical direction; the first computational level for  $\tilde{u}$  and  $\tilde{v}$  is located at elevation  $\frac{1}{2} \Delta_z$ .

Here, we consider cubic roughness cases with  $h/H = 1/4$  and  $1/8$  (SC1 and SC2). For cases SC1 and SC2, the cube spacing is a block height (i.e.  $s/h = 1$ ). We also consider six cases of homogeneous momentum roughness,  $z_0$  (U1 to U6). The computational mesh for all cube simulations is discretised with  $N_x = N_y = N_z = 128$ , while the homogeneous roughness cases are adequately resolved with  $N_x = N_y = N_z = 64$ . [34] Table 1 summarises the simulation attributes, where  $L/H$  is the domain horizontal length (streamwise and spanwise extent equal for all cases). We record time series of streamwise,  $\tilde{u}/u_\tau$ , and vertical,  $\tilde{w}/u_\tau$ , velocity at all vertical computational levels across the depth of the boundary layer at positions  $x_1$  to  $x_4$  for the cube cases (Figure 1(b)). Since the urban topography cube height is uniform, selecting positions  $x_1$  to  $x_4$  ensures that we capture representative data at all other ‘cell-centred’ positions. For the homogeneous roughness cases, we record time-series data at the geometric centre of the domain.

The immersed boundary method (IBM) used here is based on a wall model, which depletes momentum based on the unit-normal area on which the flow impinges [33,38] and the associated drag is added as a body force in the momentum transport equation. For cases U1 to U6 (homogeneous rough), the equilibrium logarithmic law [39,40] is used exclusively to impose aerodynamic drag:

$$\frac{\tau_{i3}^w}{\rho} = u_\tau^2 = - \left[ \frac{\kappa U}{\ln(z/z_0)} \right]^2 \frac{\hat{u}_i}{U}, \quad (3)$$

where  $i = 1$  and  $2$  corresponds with the streamwise and spanwise, respectively,  $\kappa$  is the von Kármán constant ( $\kappa = 0.4$ ),  $z_0$  is a (momentum) roughness length,  $\tilde{u}_i$  and  $\hat{u}_i$  denote grid- and test-filtered quantities, respectively, and  $U(x, y) = [\hat{u}^2(x, y) + \hat{v}^2(x, y)]^{1/2}$  is magnitude of the local test-filtered velocity. See Table 1 for the particular roughness lengths used. Here, we follow Bou-Zeid et al. [34] by using the test-filtered velocities for computing the wall stress (Equation (3)). This approach is typically used for modelling flows over heterogeneous [41] or complex [33] topographies, since it serves to reduce variance of the streamwise and spanwise velocity components close to the wall, thereby improving prediction of the logarithmic law. For cases SC1 and SC2 (Table 1), we use the equilibrium logarithmic law for regions with  $h(x, y) = 0$  (Equation (3)) in conjunction with an IBM for regions with  $h(x, y) > 0$ . The present IBM technique imposes aerodynamic drag owing to the obstacles by computing a body force,  $\mathbf{f}$ , in Equation (1) due to spatial variation of the topography,  $h(x, y)$ . For regions where  $h(x, y) > \Delta_z/2$ , the orographic drag force imposed on the flow by  $h(x, y)$  is

$$\mathbf{F} = - \int_S p^w \mathbf{n} dS, \quad (4)$$

where  $n_i$  is the unit normal vector to  $h(x, y)$  and  $p^w$  is the resolved wall pressure acting on  $h(x, y)$ . This IBM technique (previously named the gradient-based drag modelling technique, Anderson and Meneveau [33], and later, Anderson [38]) is used to model pressure drag forces due to  $p^w$ . After division by density,  $\rho$ , and local computational cell volume,  $\Delta_x \Delta_y \Delta_z$ , Equation (4) reduces to a drag force per unit mass required in Equation (1):

$$\frac{1}{\rho} \mathbf{f} = - \frac{1}{\rho \Delta^2 \Delta_z} \int_S p^w \mathbf{n} dS \approx -\tilde{\mathbf{u}} R (\tilde{\mathbf{u}} \cdot \nabla h) \frac{1}{\Delta_z}, \quad (5)$$

where  $R(x)$  is the ramp function ( $R(x) = x$  if  $x \geq 0$ , and  $R(x) = 0$  if  $x < 0$ ) and  $\partial h / \partial x_k$  ( $k = 1$  and  $2$ ) is the gradient of  $h(x, y)$  in the  $x$  and  $y$  directions. This use of the ramp function isolates frontal areas of  $h(x, y)$  on which  $\tilde{u}_i$  impinges. We assume the drag coefficient,  $C_d = 2$ , for all cases, and therefore the typical  $\frac{1}{2} C_d$  factor is omitted in Equation (5) (this implies complete depletion of incoming momentum). The approach was tested against numerous data-sets available in the literature for flow over different kinds of topography – blocks, sinusoids, ellipsoidal mounds – and in all cases the performance was satisfactory (agreement of time- and plane-averaged streamwise velocity profiles within 10%). The Anderson and Meneveau [33] technique is somewhat unique, as it is used to specify drag imposed by topography resolved in the horizontal directions but not the vertical (i.e.  $h(x, y)$  does not exceed the height of the first computational mesh level,  $\Delta_z/2$ ). Here we use the vertically resolving version of this modelling approach, [38] where Equation (5) models drag associated with ‘cut’ cells while the velocity at fully immersed, internal cells is set to zero. For comparison of time- and plane-averaged flow statistics from this modelling technique against literature data-sets for a variety of topographies, the interested reader may consult Anderson [38].

All velocities are normalised by shear velocity,  $u_\tau$ . For cases U1 to U6, shear velocity is determined simply as  $u_\tau = (\tau_{13}^w / \rho)^{1/2}$ ; for cases SC1 and SC2, shear velocity is determined based on the maximum Reynolds shearing stress occurring in the roughness sublayer:

$$u_\tau = \max_z ([\langle \tilde{u}' \tilde{w}' \rangle_{x,y,t} + \langle \tau_{xz} \rangle_{x,y,t}]^{1/2}), \quad (6)$$

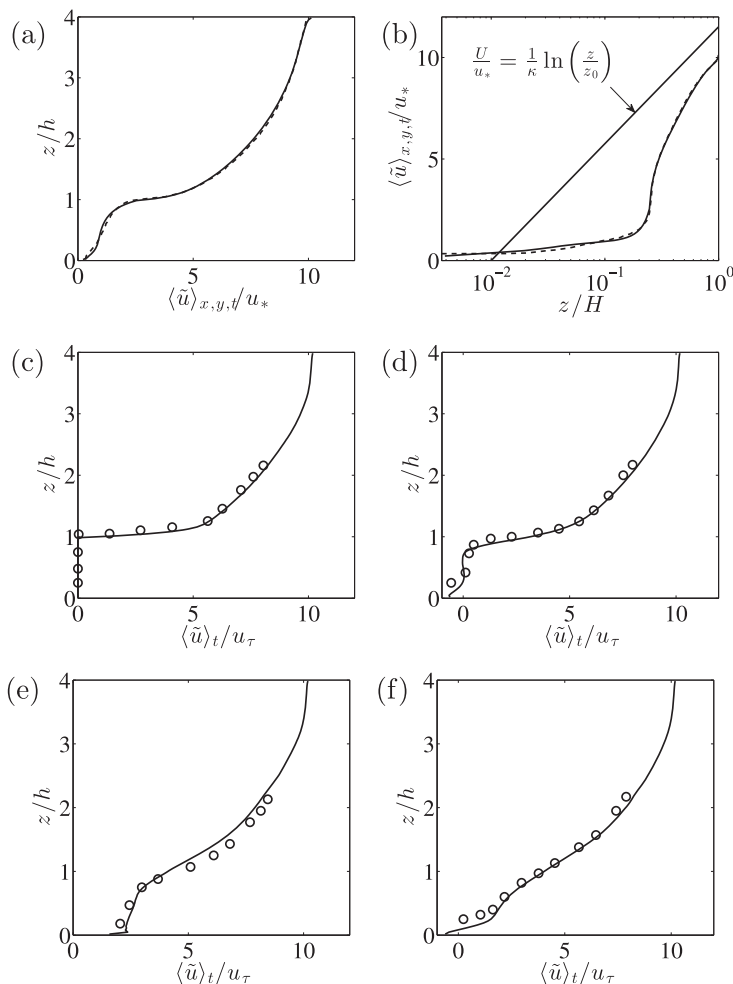


Figure 3. Vertical profiles of time- and plane-averaged streamwise velocity (solid: present LES; dashed: direct numerical simulation by Coceal et al. [8]) in linear-linear axis scaling (a) and logarithmic-linear axis scaling (b). In panel (b), a logarithmic profile is included (see figure annotation) for  $z_0/H = 10^{-2}$ . Vertical profiles of time-averaged streamwise velocity: (c) position  $x_1$  in Figure 1(b); (d) position  $x_2$  in Figure 1(b); (e) position  $x_3$  in Figure 1(b); and (f) position  $x_4$  in Figure 1(b). In panels (c) to (f), solid line and circles denote results from present LES and experiments (Cheng and Castro [6], case ‘C20S’), respectively.

where shearing stress associated with resolved fluctuations is evaluated under the horizontal statistical heterogeneity condition, [3,5]  $\tilde{\mathbf{u}}' = \tilde{\mathbf{u}} - \langle \tilde{\mathbf{u}} \rangle_{x,y,t}$ , and  $\langle \dots \rangle_a$  denotes averaging over dimension  $a$ . In spite of concerns posed by this approach owing to mean flow spatial gradients in the sublayer, we have used this approach and accomplished close agreement with the literature data-sets, as shown in Figure 3. We stress that for cases SC1 and SC2,  $z_0$  is based on regions with  $h(x, y) = 0$ ; additional aerodynamic drag due to the obstacles ( $h(x, y) > 0$ ) is imposed with the IBM. In Section 3.2, discussion regarding the ‘effective’ roughness length,  $z_{0, \text{eff}}$ , for cases SC1 and SC2 is provided (also summarised in Table 2).

In order to demonstrate fidelity of the IBM [38] technique used within the present LES (Equation (1)) for resolving sublayer turbulence, results of a validation case are

Table 2. Summary of simulation results.  $z_{0, \text{Eff.}}/H$  is evaluated by fitting a logarithmic velocity profile with varying  $z_0$  to plane-averaged streamwise velocity profiles from LES.

Name	$z_{0, \text{Eff.}}/H$	$\approx z_{\text{Ref.}}/H$
SC1	$5.412 \times 10^{-3}$	0.130
SC2	$1.08 \times 10^{-2}$	0.254
U1	$1 \times 10^{-3}$	0.012
U2	$1 \times 10^{-2}$	0.023
U3	$1 \times 10^{-3}$	0.023
U4	$1 \times 10^{-4}$	0.023
U5	$1 \times 10^{-5}$	0.023
U6	$1 \times 10^{-6}$	0.023

presented here. The case is in fact SC2 from Table 1; the literature data-sets are sourced from Cheng and Castro [6] (wind tunnel) and Coceal et al. [8] (DNS). Although the present LES Reynolds number is much larger than for the experimental and DNS data-sets, all the below comparison is performed with outer-scaled statistics. Since outer-scaled turbulence statistics exhibit Reynolds number dynamic similarity ('fully rough' conditions [42]), meaningful comparison between the present LES results and literature data-sets from DNS or experiments can be made (Figure 3). Figure 1(b) shows a plan view of the topography, where the flow direction is aligned in the  $x$ -direction. Figure 1 shows locations  $x_1, x_2, x_3,$  and  $x_4$ , at which vertical profiles of time-averaged streamwise velocity,  $\langle \tilde{u} \rangle_t / u_\tau$ , are provided in the literature data-sets. [6,8] Figure 3 shows vertical profiles of  $\langle \tilde{u} \rangle_t / u_\tau$  from the present LES (solid line), along with experimental [6] (circles) and DNS [8] (dashed line). Figure 3(b) shows Figure 3(a) profile, plotted in logarithmic-linear axis scaling; for discussion, a logarithmic profile has been added, to illustrate that the LES profile (solid, curved line) tends to a logarithmic for  $z/H \gtrsim 0.5$  (or  $z/h \gtrsim 2$ ).

### 3. Results

#### 3.1. Time–height contours

Figure 4 shows time–height colour contours of streamwise (a) and vertical (b) velocity fluctuations at position  $x_1$  (Figure 1(b)) for case SC1 (Table 1); fluctuation is defined as deviation of a quantity from its time average:

$$\tilde{u}'(\mathbf{x}, t) = \tilde{u}(\mathbf{x}, t) - \langle \tilde{u}(\mathbf{x}, t) \rangle_t. \quad (7)$$

In addition, we apply quadrant analysis [4,43] to the  $x - z$  component Reynolds shearing stresses (i.e.  $\{\tilde{u}', \tilde{w}'\}$ ), to illustrate the temporal dynamics of turbulent momentum fluxes in the urban roughness sublayer. Following is the established nomenclature, [43,44] we define the four quadrants as

$$\begin{aligned}
 Q1 \text{ (Outward interaction): } & \tilde{u}' > 0 \text{ and } \tilde{w}' > 0, \\
 Q2 \text{ (Ejection): } & \tilde{u}' < 0 \text{ and } \tilde{w}' > 0, \\
 Q3 \text{ (Inward interaction): } & \tilde{u}' < 0 \text{ and } \tilde{w}' < 0, \text{ and} \\
 Q4 \text{ (Sweep): } & \tilde{u}' > 0 \text{ and } \tilde{w}' < 0.
 \end{aligned} \quad (8)$$

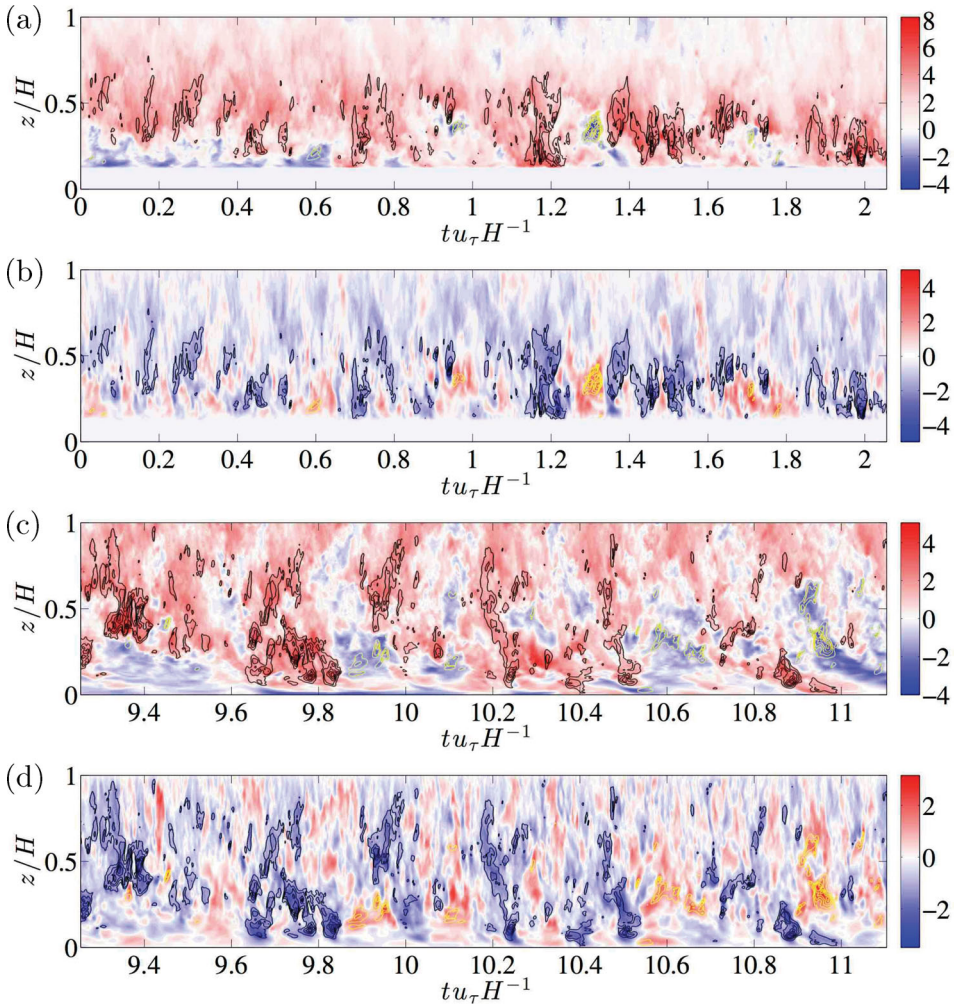


Figure 4. Time–height contours of fluctuating velocity ( $\tilde{\mathbf{u}}'(\mathbf{x}, t) = \tilde{\mathbf{u}}(\mathbf{x}, t) - \langle \tilde{\mathbf{u}}(\mathbf{x}, t) \rangle_t$ ) components for case SC1 (Table 1) at positions indicated in Figure 1(b): (a)  $\tilde{u}'(x_1, y_1, z, t)$  at  $x_1$ ; (b)  $\tilde{w}'(x_1, y_1, z, t)$  at  $x_1$ ; (c)  $\tilde{u}'(x_4, y_4, z, t)$  at  $x_4$ ; and (d)  $\tilde{w}'(x_4, y_4, z, t)$  at  $x_4$ . In addition to colour floods, line contours denote contributions to  $x - z$  component of Reynolds shearing stresses,  $\tilde{u}'\tilde{w}'$ , due to  $Q4$  ‘sweep’ (black) and  $Q2$  ‘ejection’ (yellow) events. Note that in panels (a) and (b),  $\tilde{\mathbf{u}}'(x, y, z/H < 1/8, t) = 0$  owing to the presence of cubes of height  $h/H = 1/8$ .

Note that in Figures 4, 5, and 6, dimensional time has been ‘shear normalised’ by the prescribed shear velocity,  $u_\tau$  and boundary layer depth,  $H$ . Unless noted otherwise, this time normalisation is used hereafter. Also, we add that colour floods at positions  $x_1$  and  $x_4$  are shown since these represent the limiting cases ( $x_2$  and  $x_3$  are intermediate, as seen in Figure 1(b)). Additional statistics below incorporate all positions.

At each vertical position,  $z$ , we determine the contribution from quadrant 1 to 4 events to the overall turbulent stress based on

$$\langle \tilde{u}'\tilde{w}' \rangle_{t,Q}(\mathbf{x}_l, z, t; \mathcal{H}) = \langle \tilde{u}'(\mathbf{x}_l, z, t)\tilde{w}'(\mathbf{x}_l, z, t)I_Q(\mathbf{x}_l, z; \mathcal{H}) \rangle_t, \quad (9)$$

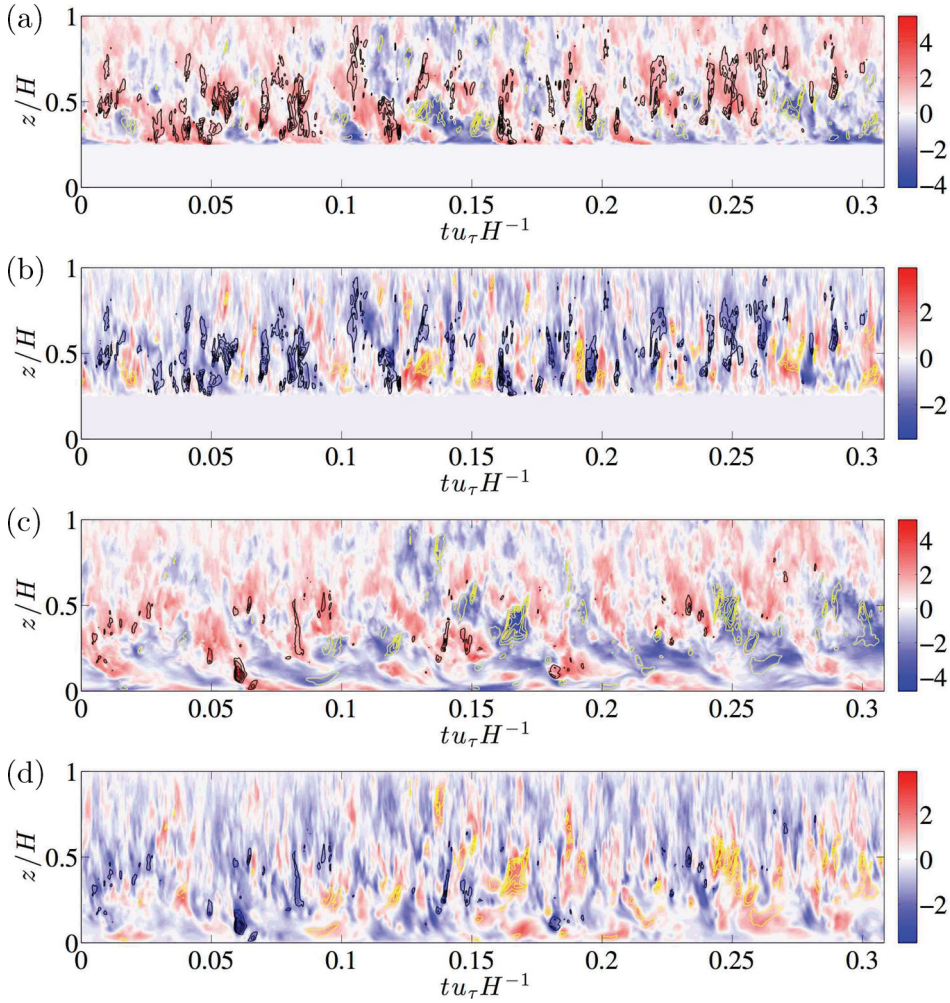


Figure 5. Time–height contours of fluctuating velocity ( $\tilde{\mathbf{u}}'(\mathbf{x}, t) = \tilde{\mathbf{u}}(\mathbf{x}, t) - \langle \tilde{\mathbf{u}}(\mathbf{x}, t) \rangle_t$ ) components for case SC2 (Table 1) at positions indicated in Figure 1(b): (a)  $\tilde{u}'(x_1, y_1, z, t)$  at  $x_1$ ; (b)  $\tilde{w}'(x_1, y_1, z, t)$  at  $x_1$ ; (c)  $\tilde{u}'(x_4, y_4, z, t)$  at  $x_4$ ; and (d)  $\tilde{w}'(x_4, y_4, z, t)$  at  $x_4$ . In addition to colour floods, line contours denote contribution to  $\tilde{u}'\tilde{w}'$  due to  $Q4$  ‘sweep’ (black) and  $Q2$  ‘ejection’ (yellow) events. Note that in panels (a) and (b),  $\tilde{\mathbf{u}}'(\mathbf{x}, y, z/H < 1/4, t) = 0$  owing to the presence of cubes of height  $h/H = 1/4$ .

where  $\mathbf{x}_i \equiv$  local (two-dimensional) positions,  $x_1, x_2, x_3$  or  $x_4$  (see Figure 1(b)),  $\mathcal{H}$  is the so-called hole size and used to specify threshold,  $T$ , on the magnitude of terms contributing to the turbulent stresses, subscript  $Q$  denotes the quadrant event of interest (i.e. sweep or ejection, Equation (8)), and  $I_Q(x_j, z; \mathcal{H})$  is the indicator function which is used to isolate the role of different events based on their magnitude (or some predefined criteria):

$$I_Q(x_j, z; \mathcal{H}) = \begin{cases} 1 & \text{if } |\tilde{u}'(x_j, z)\tilde{w}'(x_j, z)|_Q \geq T, \text{ and} \\ 0 & \text{if } |\tilde{u}'(x_j, z)\tilde{w}'(x_j, z)|_Q < T, \end{cases} \quad (10)$$

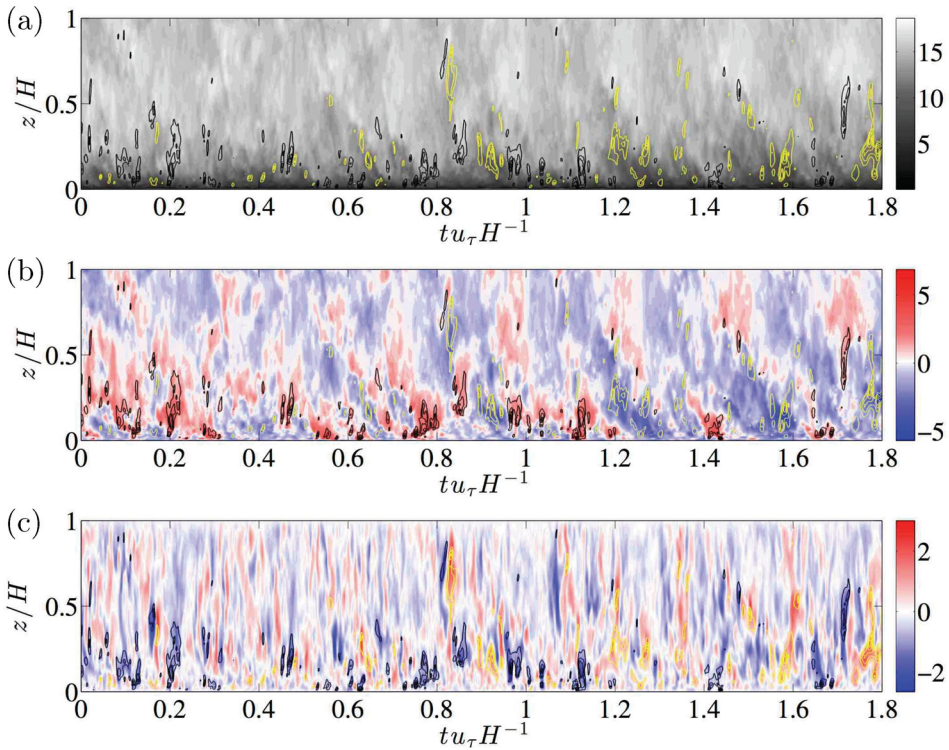


Figure 6. Time–height contours of resolved and fluctuating velocity for flow over homogeneous rough surface, case U1, taken from centre of surface: (a)  $\tilde{u}(x_c, y_c, z, t)/u_\tau$ ; (b)  $\tilde{u}'(x_c, y_c, z, t)/u_\tau = \tilde{u}(x_c, y_c, z, t)/u_\tau - \langle \tilde{u}(x_c, y_c, z, t) \rangle_t / u_\tau$ ; and (c)  $\tilde{w}'(x_c, y_c, z, t)/u_\tau = \tilde{w}(x_c, y_c, z, t)/u_\tau - \langle \tilde{w}(x_c, y_c, z, t) \rangle_t / u_\tau$ . In addition to colour floods, line contours denote contribution to  $\tilde{u}'\tilde{w}'$  due to  $Q4$  ‘sweep’ (black) and  $Q2$  ‘ejection’ (yellow) events.

where, in this study,  $T = \mathcal{H} = 0$ , although alternative criteria can be used to define the threshold.[44] By selecting  $T = 0$ , the contribution of all events to  $\langle \tilde{u}'\tilde{w}' \rangle_t$  is considered. This is appropriate for the present purposes, since we wish to demonstrate how turbulent mixing in the roughness sublayer varies with the passage of coherent, outer layer motions. For boundary layer turbulence, the ejection ( $Q2$ ) and sweep ( $Q4$ ) events are most relevant to the shear stress, while the contributions from  $Q1$  and  $Q3$  events are known to be rather modest.[44] Moreover, in the roughness sublayer it is known that contributions to shear stresses associated with  $Q4$  events exceed  $Q2$  [4,8,10]; in the aloft logarithmic region,  $Q2$  stresses exceed  $Q4$ . Thus, Figure 4(a) and 4(b) contains rich information on the temporal dynamics of turbulence above cubical topographies. First, Figure 4(a) ( $\tilde{u}'$ ) shows a clear, repetitive advective lag in the  $\tilde{u}'$  time series, illustrated by negatively inclined low(blue)- and high(red)-momentum structures. Thus, there is a time lag between the passage of coherent structures in the outer layer and detection of their effects in the roughness sublayer, which hereafter is called an advective lag. Figure 4(c) and 4(d) show the same flow quantities for point  $x_4$  (Figure 1(b)). Here, the  $\tilde{u}'$  advective delay is even more prevalent, a result of coherent ‘roller’ motions produced at the cubes [16] ( $x_1$ ) and advecting downwind [8] while remaining within the sublayer. We contend that the onset of such a momentum excess (in the outer layer) precedes a sublayer ‘spike’ in Reynolds shear stresses associated with a  $Q4$  event. Rollers play an important role, since they are contained within the roughness sublayer

and facilitate downward momentum fluxes leading to elevated Reynolds stresses owing to sweeps. Likewise, the passage of LMRs in the outer layer precedes periods of relatively subdued mixing in the roughness sublayer. For example, consider the event beginning at  $\{tu_\tau H^{-1}, z/H\} \approx \{10.2, 0.78\}$  and the subsequent advective lag before excitation at the cube height,  $\{tu_\tau H^{-1}, z/H\} \approx \{10.3, 0.1\}$  (Figure 4(c)). The sublayer excitation corresponds with significant  $Q4 \tilde{u}' \tilde{w}'$ . Consultation of Figure 4(d) shows the alternating sign of  $\tilde{w}'$  and the congruence of this with  $\tilde{u}' \tilde{w}'$ . To this extent, we note that  $\tilde{w}'$  does not exhibit an advective delay. We note also that the sampling period duration for Figure 4(a)–(b) is very similar,  $tu_\tau H^{-1} \approx 2$ ; we showed different sampling periods for generality. This is true also for subsequent results, shown below.

Finally, we emphasise here that periods of  $\tilde{u}' \neq 0$  in the inertial layer ( $z/H \gtrsim 4h/H \approx 0.5$ ) are associated with the passage of coherent, quasi-streamwise-elongated coherent motions [8,25] in the outer layer. Thus, it is interesting to note an apparent inner–outer coupling between the passage of such logarithmic structures and the excitation and subdual of sublayer mixing. One is reminded of the amplitude modulation findings developed for smooth wall turbulent boundary layers regarding the ‘imprint’ of large-scale, outer layer structures on near wall motions [45–48] (discussion to follow below). Specifically, Mathis et al. [48] demonstrated that inner (viscous) layer streamwise velocity fluctuations are subjected to an amplitude modulation by the passage of outer (logarithmic) layer coherent structures. They developed a predictive model for this amplitude modulation, which required inputs only from the outer layer (and experimentally determined empirical parameters). The results presented heretofore suggest the presence of an analogous amplitude modulation process for rough wall flows.

Figure 5 shows time–height contours for case SC2 (Table 1) at positions  $x_1$  and  $x_4$  (Figure 1(b)). This case is identical to SC1 (Figure 4), except that the cubes are effectively doubled in size (i.e.  $H/h = 4$  and, therefore,  $L/h = 8$  or  $L/H = 2$ ; these case attributes are summarised in Table 1). Nonetheless, we observe similar advective lag in the  $\tilde{u}'$  time–height colour floods (Figure 5(b) and 5(d)). We also observe that the passage of a coherent structure,  $\tilde{u}' > 0$ , in the inertial layer, say  $z/H \approx 0.75$ , manifests in the roughness sublayer and canopy (Figure 5(c)) at a later time. Likewise, it is evident that elevated Reynolds stresses owing to sweeps at the cube height,  $h/H = 1/4$ , are generally preceded by the aloft passage of coherent  $\tilde{u}' > 0$  parcels in the logarithmic layer. We observe similar  $\tilde{w}'$  patterns for this case, with only mild advective lag relative to the  $\tilde{u}'$ .

Finally, it is of interest to contrast Figures 4 and 5 cubical roughness results against those for case U1, a homogeneous rough wall (Figure 6). For case U1, drag is exclusively imposed via the equilibrium logarithmic law (Equation (3)). We selected  $z_0$  for case U1 to closely match the effective roughness length,  $z_{0, \text{eff}}$ , for case SC2 (where  $z_{0, \text{eff}}$  is evaluated by fitting a logarithmic streamwise velocity profile to the inertial-layer velocity profile). Table 2 summarises  $z_{0, \text{eff}}$  for all cases in this study, where  $z_{0, \text{eff}} = z_0$  for cases U1 to U6. Thus, for case U1, the roughness sublayer and canopy processes responsible for momentum depletion are all parameterised by the equilibrium logarithmic law. Nevertheless, we report similar patterns in the time–height colour floods. Figure 6(a) shows the resolved streamwise velocity,  $\tilde{u}$ , which is included here to demonstrate that the homogeneous rough case possesses the kinds of temporal structural attributes observed for flow over cubes, even though a roughness sublayer is not resolved. Figure 6(b) and 6(c) show  $\tilde{u}'$  and  $\tilde{w}'$ , respectively. Advective lag of  $\tilde{u}'$  is apparent in the time–height contours, as is the relative maxima in sweep-driven Reynolds stresses at the ‘conclusion’ of a  $\tilde{u}' > 0$  coherent motion. It is apparent for this case also that the  $\tilde{w}'$  contours exhibit negligible advective lag.

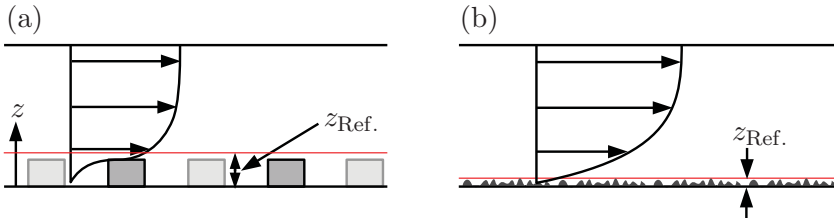


Figure 7. Sketch showing: (a) cube topography (SC1 to SC2, Table 1) and (b) homogeneous roughness transect and indication of reference elevation,  $z_{\text{Ref}}$ . (U1 to U6, Table 1).

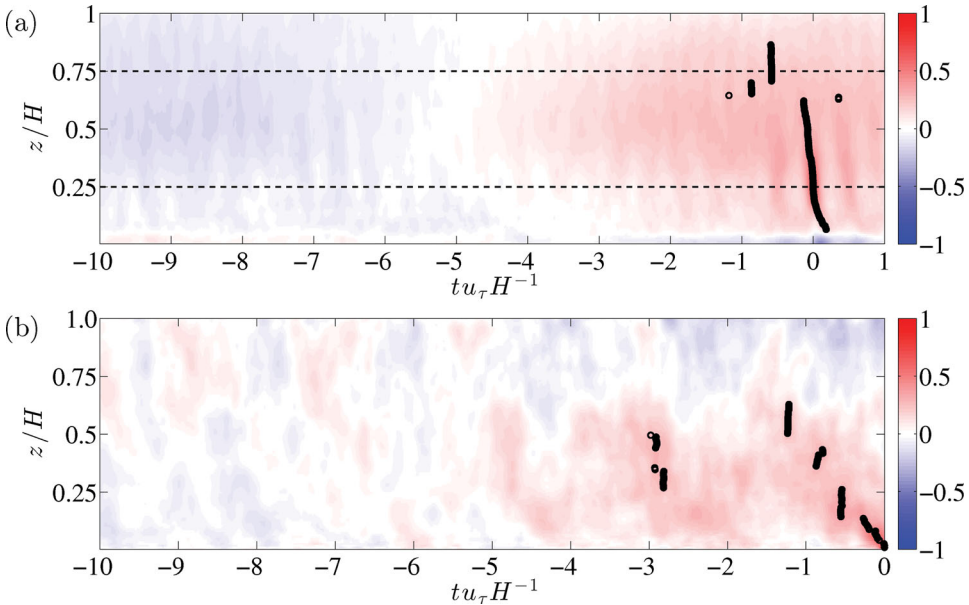


Figure 8. Correlation coefficient,  $\gamma_{uu}(\mathbf{x}_l, z, \tau; z_{\text{Ref.}})$  (Equation (11)), for cases SC2 (position  $x_4$ , panel a) and U1 (panel b). Black markers denote shear normalised maximum advective lag,  $\tau_{\text{max},u\tau}H^{-1}$  (Equation (12)).

### 3.2. Advective lag computation

We quantify the  $\tilde{u}'$  advective lag qualitatively observed in Figures 4–6. This is accomplished in two steps. First, we must select a reference height,  $z_{\text{Ref.}}$ , at which a reference data-set can be collected. Figure 7 is a sketch of the cubic topography and homogeneous roughness cases, with indication of the selected  $z_{\text{Ref.}}$  positions. Precise  $z_{\text{Ref.}}$  values are presented in Table 2. We selected  $z_{\text{Ref.}}$  to be slightly above the ‘top’ of the roughness. We adopted this approach since it facilitates comparison between these fundamentally different topographies. From here, we compute correlations maps as the convolutions:

$$\gamma_{uu}(\mathbf{x}_l, z, \tau; z_{\text{Ref.}}) = (\tilde{u}'(\mathbf{x}_l, z, t)I\tilde{u}'(\mathbf{x}_l, z_{\text{Ref.}}, t))(\tau) = \int_{-\infty}^{\infty} \tilde{u}'(\mathbf{x}_l, z, t)\tilde{u}'(\mathbf{x}_l, z_{\text{Ref.}}, t + \tau)dt, \quad (11)$$

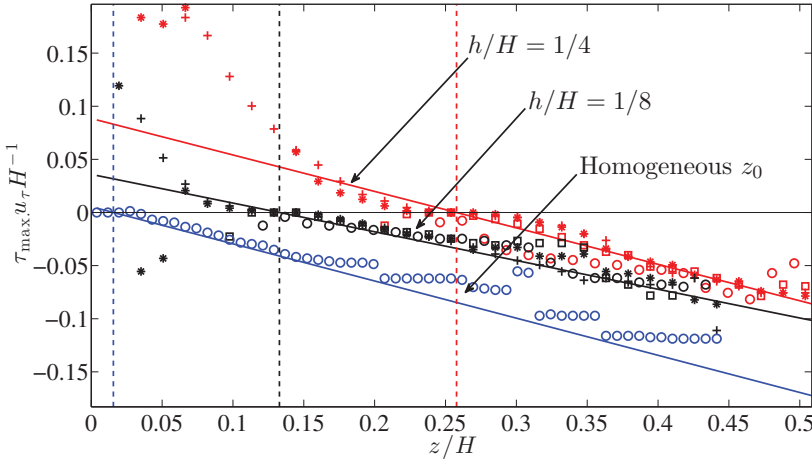


Figure 9. Advective lag versus wall-normal elevation for cases U1 (blue symbols), SC1 (black symbols), and SC2 (red symbols). For cases SC1 and SC2, symbols correspond with:  $x_1$  (circles),  $x_2$  (squares),  $x_3$  ('plus' sign), and  $x_4$  (asterisk). Blue symbols correspond with  $x_c$  for the homogeneous rough case. Vertical dashed lines denote  $z_{\text{Ref.}}$  for different cases (dashed blue: U1; dashed black: SC1; and dashed red: SC2). Solid lines represent Equation (17) predictions of time-lag for effective roughness lengths summarised in Table 2.

where  $\mathbf{x}_l$  represents a spatial ( $x - y$ ) position (Figure 1(b)). Figure 8(a) and 8(b) show  $\gamma_{uu}(\mathbf{x}_l, z, \tau; z_{\text{Ref.}})$  for cases SC2 and U1, respectively. In Figure 8(a), the lower and upper horizontal dashed black lines represent the cube height and three times the cube height, respectively (where three cube heights is approximately equal to the roughness sublayer depth). It is clear that both data-sets exhibit an advective lag, as evidenced by positive correlation with aloft preceding events. We also observe similar patterns for the cubic and homogeneous rough cases, which is consistent with observations of Figures 5(c) and 6(b). We compute advective lag as

$$\tau_{\max.}(z; z_{\text{Ref.}}) = \arg \max_t ((\tilde{u}'(\mathbf{x}_l, z, t) I \tilde{u}'(\mathbf{x}_l, z_{\text{Ref.}}, t))(t)), \quad (12)$$

where  $\arg \max$  denotes the value  $t$  for which the convolution is strongest. We discard  $\tau_{\max.}$  values corresponding with  $\gamma_{uu}(\mathbf{x}_l, z, \tau_{\max.}; z_{\text{Ref.}}) < \chi$ , where  $\chi = 0.3$  is a predefined threshold. We experimented with a range of  $\chi$  values, finding generally that increasing the threshold only serves to remove spurious values for  $z > z_{\text{Ref.}}$  while the underlying  $\tau_{\max.}(z; z_{\text{Ref.}})$  trends were robust and indifferent to  $\chi$ . Figure 9 shows shear normalised advective lag,  $\tau_{\max.} u_{\tau} H^{-1}$  for cases SC1, SC2, and U1 (case attributes found in Table 1). For cases SC1 and SC2, it is clear that positions  $x_1$  to  $x_4$  exhibit effectively the same  $\tau_{\max.} u_{\tau} H^{-1}$  profiles. Above  $z_{\text{Ref.}}$ , the profiles are roughly linear, and we remind the reader that  $z_{\text{Ref.}}$  is the approximate obstacle elevation (or centre of the mean streamwise velocity profile inflection). Furthermore, the advective lag is always negative above  $z_{\text{Ref.}}$ , which is precisely consistent with qualitative observations in Figures 4–6. For position  $x_1$ , there of course are no  $\tau_{\max.} u_{\tau} H^{-1}$  datapoints below  $z_{\text{Ref.}}$  due to the solid cube. A few datapoints are available for position  $x_2$ , owing to its position in the lee of the cubes. However, at positions  $x_3$  and  $x_4$ , a broad range of  $\tau_{\max.} u_{\tau} H^{-1}$  values are available. We emphasise also that the  $\tau_{\max.} u_{\tau} H^{-1}$  values in Figure 9 are only associated with  $\gamma_{uu} > \chi$  (i.e. they represent only

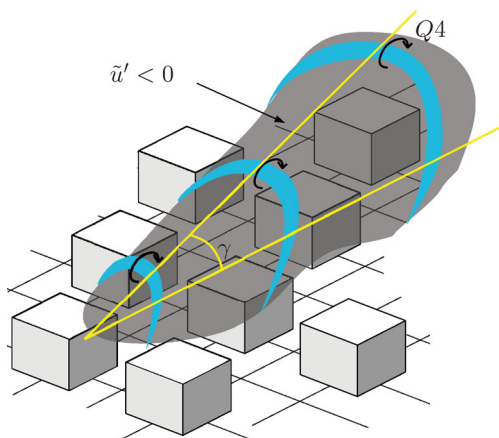


Figure 10. Sketch of low-momentum region (LMR) above array of cubes. The LMR,  $\tilde{u}' < 0$ , is denoted by transparent grey. Encapsulating the LMR are hairpins (blue). The LMR is inclined at angle,  $\gamma$ , and the hairpin heads exhibit positive spanwise vorticity (sketch denotes sweep event,  $Q4$ ). The individual hairpin ‘legs’ would themselves be inclined at  $\approx 45^\circ$ . [24]

strongly correlated datapoints). Thus, the approximate linearity,  $\tau_{\max.} \sim -z$  for  $z > z_{\text{Ref.}}$ , is a product of actual processes within the roughness sublayer and inertial layer. In the following subsections, we provide a conceptual explanation and scaling argument for the underlying dynamics responsible for the advective lag reported in Figure 9.

### 3.3. Passage of coherent motions

The presence of meandering, coherent parcels of relatively low and high momentum in turbulent wall-bounded flows over smooth [20–24,26,27] and rough [8,25,50,51] walls is well known. The LMRs are encapsulated by hairpin packets at the interface between regions of differing momentum. [24,28] For the case of cube roughness such as the cases considered here, Figure 10 is a sketch of the aforementioned structural attributes. A streamwise-vertical transect through the LMR would reveal a typical inclination of  $\gamma \approx 15^\circ$ . [8,20,25,52] Quantitative visualisation of Figure 10 dynamics can also be attained with vortex visualisation techniques.

Here, we compute swirl strength,  $\lambda_{ci}$ , of the instantaneous three-dimensional velocity field,  $\tilde{\mathbf{u}}$ . [20,53–55] Swirl strength is computed by first evaluating the velocity gradient tensor,  $\mathbf{A} = \nabla \tilde{\mathbf{u}}$ , and computing its eigenvalues.  $\lambda_{ci}$  is the imaginary component of the second eigenvalue of  $\mathbf{A}$ . From this, we obtain the signed swirl strength,  $\lambda_{ci}^*$ , simply based on the vorticity component of interest. In the following, we wish to study streamwise-wall normal vortical activity, so spanwise vorticity,  $\omega_y = \partial \tilde{u} / \partial z - \partial \tilde{w} / \partial x$ , is the apropos vorticity component with which to sign  $\lambda_{ci}$ :

$$\lambda_{ci}^* = \lambda_{ci} \frac{\omega_y}{\|\omega_y\|}. \quad (13)$$

Swirl strength is an illuminating tool for studying vortical activity, since it resolves only rotation and not shear. Figure 11 shows contours of  $\lambda_{ci}^*$  superimposed on vector fields of fluctuating velocity components,  $\{\tilde{u}', \tilde{w}'\}$ . The figures clearly show the presence of LMRs beneath a series of hairpin heads (evidenced by local regions of elevated  $\lambda_{ci}^*$ ). Figure 11(a) is for case

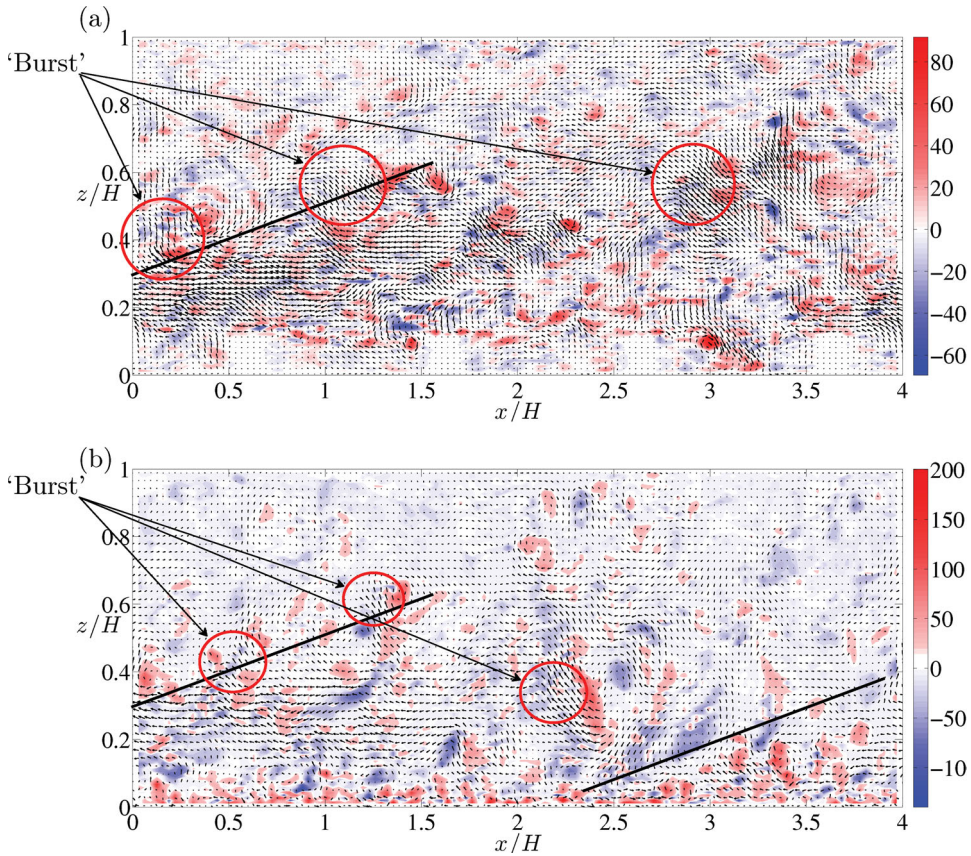


Figure 11. Transects of flow field statistics for: (a) case SC1 and (b) case U1. Vectors denote fluctuating velocity components,  $\{\tilde{u}', \tilde{w}'\}$ , while colour contours are signed swirl strength,  $\lambda_{ci}^*$  (Equation (13)). On both, the solid black line represents an approximate demarcation between an LMR (below) and an ambient fluid (above) and is inclined at  $\gamma = 15^\circ$ . Local regions of positive  $\lambda_{ci}^*$  represent the heads of hairpins above the LMR, which are followed by a  $Q2$  'burst' event,[49] as indicated above.

SC2, and the presence of immersed blocks corresponds with regions of  $\{\tilde{u}', \tilde{w}'\} \approx \{0, 0\}$ . To facilitate discussion, we have added solid black lines inclined at  $\gamma = 15^\circ$ , which is the approximate inclination angle of hairpin trains in such flows.[8,50,51] The coherent hairpin heads precede  $Q2$  burst events and we have indicated these events for discussion on the figures. Note also in Figure 11(a) the presence of canopy vortices associated with separation and cube-scale coherent motions, evidenced by elevated  $\lambda_{ci}$  contours (for example, at  $\{x/H, z/H\} \approx \{1.4, 0.15\}$  and  $\{3, 0.15\}$ ). For homogeneous roughness case U1, Figure 11(b) shows the same quantities as Figure 11(a). Again, the presence of coherent LMRs and a series of inclined hairpin heads are apparent. We emphasise finally that the Figure 11 images are taken from only one timestep during LES. However, these images are entirely representative of instantaneous flow patterns observed at other times during the simulation.

In Section 3.1 and Figure 9, we showed vertical profiles of advective lag,  $\tau_{\max} u_\tau H^{-1}$ , based on a reference elevation just above the canopy (see Figures 7 and 9). The linearity exhibited by  $\tau_{\max} u_\tau H^{-1}$  points to an underlying physical process in the roughness sublayer

and inertial layer. Here, we attribute  $\tau_{\max.} \sim -z$  scaling to the passage of regions of alternating low and high momentum in the roughness sublayer and inertial layer, as illustrated in Figure 11.

### 3.4. A model for advective lag

Following the passage of a LMR, Figure 11 shows that the first position in the domain to experience relatively higher momentum would be in the inertial layer, above the LMR. As the LMR advects downstream, relatively higher momentum would be recorded at progressively lower elevations. Since representative information is known about the macroscale attributes of these coherent motions, we below propose a simple, semi-empirical model to predict the advective lag between passage of such motions in the inertial layer and evidence of their ‘imprint’ on roughness sublayer and canopy dynamics.

If a LMR (i.e.  $\tilde{u}' < 0$ , above) has depth,  $\delta'$ , its length can be evaluated based on assumption of a hairpin train inclination angle:

$$L_s \approx \delta' / \tan(\gamma). \quad (14)$$

Furthermore, if we assume that a representative advective velocity for LMRs and high-momentum regions (HMRs) is the ‘outer’ velocity,  $U_0$ , we can use the equilibrium logarithmic law [40] and aerodynamic roughness length,  $z_0$ , to predict  $U_0$ :

$$\frac{U_0}{u_\tau} = \frac{1}{\kappa} \log \left[ \frac{H}{z_0} \right], \quad (15)$$

where  $\kappa$  is the von Kármán constant. For cases U1 to U6, a large inertial region will be resolved within the computational domain. For cases SC1 and SC2, the streamwise velocity profile will be inflected in the roughness sublayer, before exhibiting logarithmic wall-normal scaling in the inertial layer. Recall that for cases SC1 and SC2,  $h/H = 1/8$  and  $1/4$ , respectively, which may raise concern to some readers about the presumption of attaining a logarithmic profile in the computational domain (especially for SC2). Figure 3 shows mean streamwise velocity profiles (plane-averaged and local) for case SC2, and a logarithmic profile is clearly attained for  $z/h \gtrsim 2$  (Figure 3(b) shows the mean streamwise velocity profile with logarithmic-linear axis scaling, clearly demonstrating the presence of a logarithmic profile in the inertial layer). We note also Figure 5(a) from Coceal et al. [8], which shows local streamwise velocity profiles superimposed on one another and the very rapid tendency to logarithmic form about the canopy. Thus, an inertial layer exhibiting logarithmic scaling is present for all simulations considered in this work.  $\tau_{\max.}(z; z_{\text{Ref.}})$  is the advective lag between passage of a coherent motion at elevation,  $z$ , and associated modulation of processes at reference height,  $z_{\text{Ref.}}$ . Thus, Equations (14) and (15) can be combined to obtain the advective lag:

$$\tau_{\max.}(z; z_{\text{Ref.}}) = \frac{z_{\text{Ref.}} - z}{\tan(\gamma) U_0} = \frac{\kappa(z_{\text{Ref.}} - z)}{\tan(\gamma) u_\tau \log(H/z_0)}. \quad (16)$$

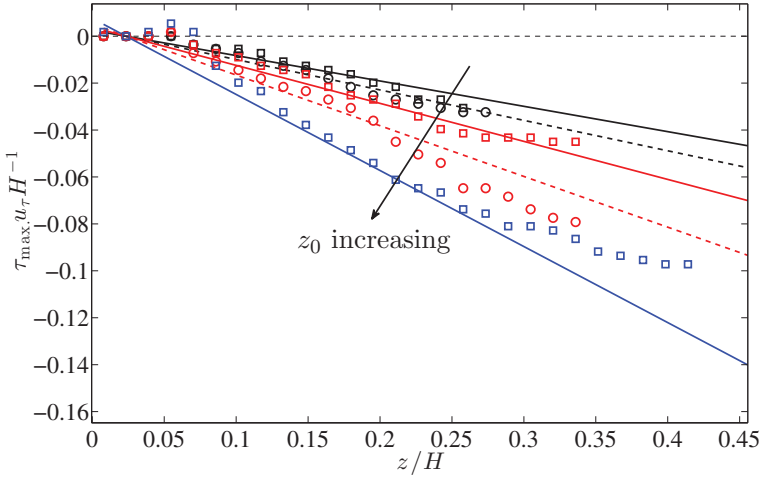


Figure 12. Vertical profiles of  $\tau_{\max}(z; z_{\text{Ref}})$  for cases U2–U6 from LES (symbols) and Equation (17) predictions (lines). Cases: U2 (blue squares, solid blue line), U3 (red circles, dashed red line), U4 (red squares, solid red line), U5 (black circles, dashed black line), and U6 (black squares, solid black line). Direction of increasing  $z_0$  is included for illustration. In the above,  $z_{\text{Ref}}/H \approx 0.023$ .

Normalising  $\tau_{\max}(z; z_{\text{Ref}})$  by friction velocity and boundary depth (‘shear normalised’) yields

$$\tau_{\max}(z; z_{\text{Ref}}) u_{\tau} H^{-1} = \frac{\kappa (z_{\text{Ref}} - z)}{\tan(\gamma) H \log(H/z_0)}. \quad (17)$$

Since we have run the LES for cases SC1 to SC2, Equation (15) can be used to retrieve an appropriate effective roughness length,  $z_{0, \text{Eff}}$ , by matching the inertial-layer profiles from LES with predictions from Equation (15). These values are summarised in Table 2<sup>2</sup>. Following deduction of  $z_{0, \text{Eff}}$ ,  $U_0$  is recorded also for substitution in Equation (17). Finally, we use  $\gamma = 15$  deg for Equation (17) predictions considered here, which is comparable to values for rough wall flows.[8,25,50–52] For cases SC1, SC2, and U1, Figure 9 shows predictions from Equation (17) (solid lines). For  $z_{\text{Ref}}/H \lesssim z/H \lesssim 0.2$ , Equation (17) predictions exhibit reasonable agreement with the LES results for case U1. This is the case of homogeneous roughness in which the roughness sublayer may be  $z/H \lesssim 0.1$ . For cases SC1 and SC2, Equation (17) predictions agree somewhat well with the LES data for  $z_{\text{Ref}}/H \lesssim z/H \lesssim 0.4$ , corresponding with 2 to 4 times the cube height. Thus, the model performance is moderately successful in the roughness sublayer and into the inertial layer. To broaden the test cases, we include Figure 12, which shows  $\tau_{\max}(z; z_{\text{Ref}})$  from cases U2 to U6 and predictions from Equation (17). Once more, we observe moderate agreement between the model and LES data for  $z_{\text{Ref}}/H \lesssim z/H \lesssim 0.2$ . Note also the apparent monotonic increase in slope of the advective lag profile,  $\partial \tau_{\max}(z; z_{\text{Ref}})/\partial z$ , with increasing aerodynamic roughness length (partial derivative here is a reference to assertions that aspects of the Equations (14)–(17) development could be generalised, for example the choice of advective velocity and inclination angle [22]). We attribute this to intensification of roughness sublayer processes with greater imposed drag. To this extent, we note that  $\partial \tau_{\max}(z; z_{\text{Ref}})/\partial z$  for case SC2 exceeds case SC1 (see Figure 9); the cube height for case SC2 is double that of SC1. Note also that  $z_{\text{Ref}}/H \approx 0.023$  for cases U2–U6 (Figure 12), although the nominated  $z_{0, \text{Eff}}/H$  varies

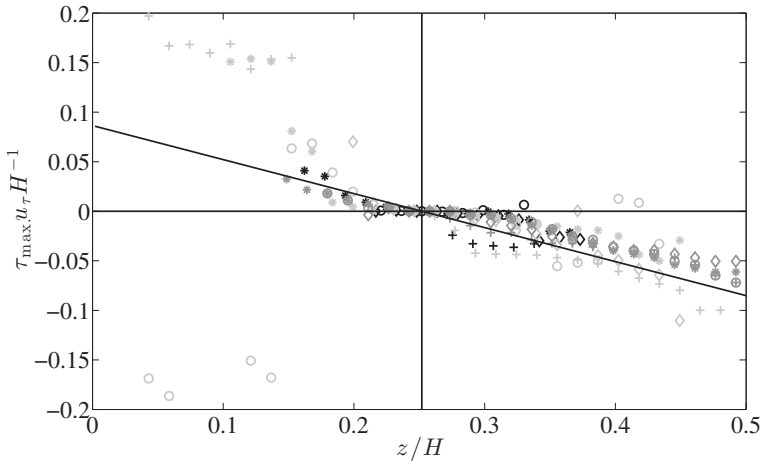


Figure 13. Vertical profiles of  $\tau_{\max}(z; z_{\text{Ref}})$  for flow over topography SC2, resolved with  $N_x = N_y = N_z = 64$  (light grey symbols),  $N_x = N_y = N_z = 128$  (dark grey symbols), and  $N_x = N_y = N_z = 256$  (black symbols). Solid black line is Equation (17) prediction with  $z_0/H = 1.08 \times 10^{-2}$  (Table 2). Symbols correspond with position  $x_1$  (+), position  $x_2$  ( $\diamond$ ), position  $x_3$  ( $\circ$ ), position  $x_4$  ( $*$ ) in Figure 1(b).

considerably. Increasing  $z_{0, \text{Eff.}}/H$  is tantamount to ‘more rough’ topographies with greater heights.

### 3.5. Resolution testing

A final component of this study involves evaluating the extent to which resolution – spatial and temporal – influences the advective lag profiles. In the results presented so far, case SC2 (Table 1) was resolved with  $N_x = N_y = N_z = 128$ . For generality, we have also modelled flow over the SC2 topography with  $N_x = N_y = N_z = 64$  and  $N_x = N_y = N_z = 256$ . The resulting advective lag profiles are shown in Figure 13, where the symbol colour corresponds with different resolutions. Included on this figure is the Equation (17) profile for the appropriate effective roughness length. It is apparent that the advective lag profiles (symbols) and model profile (solid line) exhibit the same slope. Moreover, no significant resolution dependence is apparent. As per the procedure outlined in Section 3.2, we omit advective lag computations for cases in which  $\gamma_{uu} < \chi$ .

## 4. Conclusion

LES with an IBM has been used to model neutrally stratified atmospheric boundary layer flows over urban-like topographies. We also consider a suite of cases with differing homogeneous momentum roughness, without the presence of urban-like cubes. We recorded time-series fluctuating velocity statistics across the depth of the boundary layer, providing data-sets that would typically emerge from field studies using a micrometeorological tower and series of sonic anemometers. However, owing to the use of LES, we can achieve high resolution measurements in both time and elevation (at predefined locations). With this, we considered contour maps of fluctuating streamwise and vertical velocity components with respect to shear-normalised time and elevation; superimposed on these images were

contours of Reynolds shearing stresses owing to turbulent ‘sweeps’ and ‘ejections’.[43] The colour flood contours clearly revealed the presence of an advective lag between momentum excess(deficit) in the inertial layer and excitation(subdual) of flow processes in the roughness sublayer. This advective lag was observed for all cases – cube topography and homogeneous roughness.

We computed the advective lag,  $\tau_{\max} u_{\tau} H^{-1}$ , and observed a linear scaling against elevation. This prompted consideration of underlying physics responsible for the advective lag. We used spatial flow and vortex visualisations to argue that coherent outer layer motions (LMRs and HMRs) are responsible for the advective lag between sublayer and inertial-layer dynamics. With this, we used canonical attributes of the LMRs (hairpin head inclination angle,  $\gamma$ , and advective velocity,  $U_0$ ), to develop scaling arguments for the advective lag. We observed promising results.

This work is inspired by the amplitude modulation concepts developed in recent years by Marusic and co-workers [45–48]. The existing literature on amplitude modulation is in the context of smooth wall flows (thus, ‘inner’ refers to the viscous sublayer, not the roughness sublayer). Nonetheless, it is interesting to observe some qualitative similarities in the present findings. Moreover, the present work has been performed in the context of urban-like topographies, although one could imagine applications to, for example, control of very large wind farms over which the atmospheric boundary layer is fully developed. Indeed, the modelling framework (Equation (17)) presented herein requires only two inputs:  $\gamma$  and  $z_{0, \text{Ref.}}$ . We used a somewhat standard value of  $\gamma$ , and computed  $z_{0, \text{Ref.}}$  by fitting logarithmic velocity profiles to the time- and plane-averaged streamwise velocity profiles. We expect that for urban topographies exhibiting greater height variability than the present (uniform height) cases, or for entirely different classes of complex topography, the modelling arguments presented here would be valid.

### Acknowledgements

William Anderson acknowledges support from the Army Research Office, Environmental Sciences Directorate, Atmospheric Sciences Program (Grant # W911NF-13-1-0474; PM: Drs Gordon Videen and Sandra Collier). Elie Bou-Zeid and Qi Li acknowledge support from the National Science Foundation (Grant # CBET-1058027). Computational resources were provided by Academic and Research Computing Services at Baylor University and the Texas Advanced Computing Center at the University of Texas at Austin.

### Disclosure statement

No potential conflict of interest was reported by the authors.

### Funding

William Anderson acknowledges support from the Army Research Office, Environmental Sciences Directorate, Atmospheric Sciences Program [grant number W911NF-13-1-0474] PM: Drs Gordon Videen and Sandra Collier; Elie Bou-Zeid and Qi Li acknowledge support from the National Science Foundation [grant number CBET-1058027].

### Notes

1. Throughout this study, we adopt the following nomenclature:  $\tilde{\mathbf{u}} = \{\tilde{u}, \tilde{v}, \tilde{w}\}$  is the streamwise, spanwise, and vertical velocity component, respectively;  $\mathbf{x} = \{x, y, z\}$  is streamwise, spanwise,

and vertical position, respectively; and indices (where used)  $i = 1, 2,$  and  $3$  are streamwise, spanwise, and vertical direction, respectively.

2. Alternatively, one could use predictive models for  $z_0$  based on attributes of the topography [56–58] although this would require empirical parameters.[59]

## References

- [1] Bons J, Taylor R, McClain S, Rivir R. The many faces of turbine surface roughness. *J Turbomachinery*. 2001;123:739–748.
- [2] Schultz M. Effects of coating roughness and biofouling on ship resistance and powering. *Biofouling*. 2007;23:331–341.
- [3] Calaf M, Parlange M, Meneveau C. Large eddy simulation study of scalar transport in fully developed wind-turbine array boundary layers. *Phys Fluids*. 2011;23:126603–126616.
- [4] Finnigan J, Shaw R, Patton E. Turbulence structure above a vegetation canopy. *J Fluid Mech*. 2009;637:387–424.
- [5] Belcher S, Harman I, Finnigan J. The wind in the willows: flows in forest canopies in complex terrain. *Ann Rev Fluid Mech*. 2012;44:479–504.
- [6] Cheng H, Castro I. Near wall flow over urban-like roughness. *Boundary Layer Meteorology*. 2002;104:229–259.
- [7] Belcher S, Jerram N, Hunt J. Adjustment of a turbulent boundary layer to a canopy of roughness elements. *J Fluid Mech*. 2003;488:369–398.
- [8] Coceal O, Dobre A, Thomas TG, Belcher S. Structure of turbulent flow over regular arrays of cubical roughness. *J Fluid Mech*. 2007;589:375–409.
- [9] Xie ZT, Coceal O, Castro I. Large-eddy simulation of flows over random urban-like obstacles. *Boundary Layer Meteorology*. 2008;129:1–23.
- [10] Anderson W, Chamecki M. Numerical study of turbulent flow over complex aeolian dune fields: the white sands national monument. *Phys Rev E*. 2014;89:013005/1–14.
- [11] Harmon I, Finnigan JJ. A simple unified theory for flow in the canopy and roughness sublayer. *Boundary Layer Meteorology*. 2007;123:339–364.
- [12] Böhm M, Finnigan JJ, Raupach MR, Hughs D. Turbulence structure within and above a canopy of bluff elements. *Boundary Layer Meteorology*. 2013;146:393–419.
- [13] Raupach M, Antonia R, Rajagopalan S. Rough-wall turbulent boundary layers. *Appl Mech Rev*. 1991;44:1–25.
- [14] Castro I. Rough-wall boundary layers: mean flow universality. *J Fluid Mech*. 2007;585:469–485.
- [15] Raupach M, Finnigan J, Brunet Y. Coherent eddies and turbulence in vegetation canopies: the mixing layer analogy. *Boundary Layer Meteorology*. 1996;78:351–382.
- [16] Ghisalberti M. Obstructed shear flows: similarities across systems and scales. *J Fluid Mech*. 2009;641:51–61.
- [17] Rogers M, Moser R. Direct simulation of a self-similar turbulent mixing layer. *Phys Fluids A*. 1994;6:903–922.
- [18] Finnigan J. Turbulence in plant canopies. *Ann Rev Fluid Mech*. 2000;32:519–571.
- [19] Hutchins N, Marusic I. Evidence of very long meandering features in the logarithmic region of turbulent boundary layers. *J Fluid Mech*. 2007;579:1–28.
- [20] Zhou J, Adrian R, Balachandar S, Kendall T. Mechanisms for generating coherent packets of hairpin vortices in channel flow. *J Fluid Mech*. 1999;387:353–359.
- [21] Adrian R, Meinhardt C, Tomkins C. Vortex organization in the outer region of the turbulent boundary layer. *J Fluid Mech*. 2000;422:1–54.
- [22] Christensen K, Adrian R. Statistical evidence of hairpin vortex packets in wall turbulence. *J Fluid Mech*. 2001;431:433–443.
- [23] Ganapathisubramani B, Longmire EK, Marusic I. Characteristics of vortex packets in turbulent boundary layers. *J Fluid Mech*. 2003;478:35–46.
- [24] Adrian R. Hairpin vortex organization in wall turbulence. *Phys Fluids*. 2007;19:041301.
- [25] Wu Y, Christensen KT. Spatial structure of a turbulent boundary layer with irregular surface roughness. *J Fluid Mech*. 2010;655:380–418.
- [26] Dennis D, Nickels T. Experimental measurement of large-scale three-dimensional structures in a turbulent boundary layer. Part 1. Vortex packets. *J Fluid Mech*. 2011;673:180–217.

- [27] Dennis D, Nickels T. Experimental measurement of large-scale three-dimensional structures in a turbulent boundary layer. Part 2. Long structures. *J Fluid Mech.* 2011;673:218–244.
- [28] Meinhart C, Adrian R. On the existence of uniform momentum zones in a turbulent boundary layer. *Phys Fluids.* 1995;7:694–696.
- [29] Leonardi S, Orlandi P, Djenidi L, Antonia R. Structure of turbulent channel flow with square bars on one wall. *Int J Heat Fluid Flow.* 2004;25:384–392.
- [30] Adrian R. Linking correlations and structure: stochastic estimation and conditional averaging. In: Kline S, Afgan N, editors. *Near-wall turbulence.* New York: Hemisphere Publ.; 1990.
- [31] Anderson W, Li Q, Bou-Zeid E. Numerical study of turbulence temporal characteristics in urban sublayer. Paper presented at: American Meteorological Society, Symposium on Boundary Layers and Turbulence. 21st Bi-Annual Meeting; 2014 June 9–13; Leeds, UK.
- [32] Albertson J, Parlange M. Surface length scales and shear stress: implications for land-atmosphere interaction over complex terrain. *Water Resour Res.* 1999;35:2121–2132.
- [33] Anderson W, Meneveau C. A large-eddy simulation model for boundary-layer flow over surfaces with horizontally resolved but vertically unresolved roughness elements. *Boundary Layer Meteorology.* 2010;137:397–415.
- [34] Bou-Zeid E, Meneveau C, Parlange M. A scale-dependent Lagrangian dynamic model for large eddy simulation of complex turbulent flows. *Phys Fluids.* 2005;17:025105.
- [35] Chester S, Meneveau C, Parlange M. Modelling of turbulent flow over fractal trees with renormalized numerical simulation. *J Comput Phys.* 2007;225:427–448.
- [36] Smagorinsky J. General circulation experiments with the primitive equations. *Monthly Weather Rev.* 1963;91:99–164.
- [37] Orszag S. Transform method for calculation of vector coupled sums: application to the spectral form of the vorticity equation. *J Atmospheric Sci.* 1970;27:890–895.
- [38] Anderson W. An immersed boundary method wall model for high-Reynolds number channel flow over complex topography. *Int J Numer Methods Fluids.* 2012;71:1588–1608.
- [39] Deardorff J. A numerical study of three-dimensional turbulent channel flow at large Reynolds numbers. *J Fluid Mech.* 1970;41:453–480.
- [40] Piomelli U, Balaras E. Wall-layer models for large-eddy simulation. *Ann Rev Fluid Mech.* 2002;34:349–374.
- [41] Bou-Zeid E, Parlange M, Meneveau C. On the parameterization of surface roughness at regional scales. *J Atmospheric Sci.* 2007;64:216–227.
- [42] Pope S. *Turbulent flows.* UK: Cambridge University Press; 2000.
- [43] Lu S, Willmarth W. Measurements of the structure of Reynolds stress in a turbulent boundary layer. *J Fluid Mech.* 1973;60:481–571.
- [44] Mejia-Alvarez R, Christensen K. Low-order representations of irregular surface roughness and their impact on a turbulent boundary layer. *Phys Fluids.* 2010;22:015107.
- [45] Hutchins N, Marusic I. Large-scale influences in near-wall turbulence. *Philosophical Trans Royal Soc A.* 2007;365:647–664.
- [46] Mathis R, Hutchins N, Marusic I. Large-scale amplitude modulation of the small-scale structures in turbulent boundary layers. *J Fluid Mech.* 2009;628:311–337.
- [47] Marusic I, Mathis R, Hutchins N. Predictive model for wall-bounded turbulent flow. *Science.* 2010;329:193–196.
- [48] Mathis R, Hutchins N, Marusic I. A predictive inner-outer model for streamwise turbulence statistics in wall-bounded flows. *J Fluid Mech.* 2011;681:537–566.
- [49] Sheng J, Malkiel E, Katz J. Buffer layer structures associated with extreme wall stress events in a smooth wall turbulent boundary layer. *J Fluid Mech.* 2009;633:17–60.
- [50] Hong J, Katz J, Schultz M. Near-wall turbulence statistics and low structures over three-dimensional roughness in a turbulent channel flow. *J Fluid Mech.* 2011;667:1–37.
- [51] Hong J, Katz J, Meneveau C, Schultz M. Coherent structures and associated subgrid-scale energy transfer in a rough wall turbulent channel flow. *J Fluid Mech.* 2012;712:92–128.
- [52] Krogstad PA, Antonia R. Structure of turbulent boundary layers on smooth and rough walls. *J Fluid Mech.* 1994;277:1–21.
- [53] Zhou J, Adrian R, Balachandar S. Autogeneration of near-wall vortical structures in channel flow. *Phys Fluids.* 1996;8:288–290.
- [54] Adrian R, Christensen K, Liu ZC. Analysis and interpretation of instantaneous turbulent velocity fields. *Exp Fluids.* 2000;29:275–290.

- [55] Mejia-Alvarez R, Barros J, Christensen K. Coherent flow structures at the earth's surface. Chichester, UK: John Wiley & Sons, Ltd.; 2013.
- [56] Garratt J. The atmospheric boundary layer. Cambridge, England: Cambridge University Press; 1994.
- [57] Zagarola M, Smits A. Mean-flow scaling of turbulent pipe flow. *J Fluid Mech.* 1998;373:33–79.
- [58] Anderson W, Meneveau C. A dynamic large-eddy simulation model for boundary layer flow over multiscale, fractal-like surfaces. *J Fluid Mech.* 2011;679:288–314.
- [59] Schultz M, Flack K. Turbulent boundary layers on a systematically-varied rough wall. *Phys Fluids.* 2009;21:015104.